Title

Multi-modal optimization of bismuth vanadate photoanodes via combinatorial alloying and hydrogen processing

Journal

Chemical Communications, 55(4)

ISSN

1359-7345

Authors

Newhouse, PF

Guevarra, D

Umehara, M

et al.

Publication Date

2019-01-03

DOI

10.1039/c8cc07156j

Peer reviewed

Multi-modal optimization of bismuth vanadate photoanodes *via* combinatorial alloying and hydrogen processing†

P. F. Newhouse, [a] D. Guevarra, [a] M. Umehara, [ab] D. A. Boyd,[a] L. Zhou, [a] J. K. Cooper, [cd] J. A. Haber [a] and J. M. Gregoire *[a]

Abstract: **Alloying transition metals, such as Mo, into $BiVO_4$ has emerged as the primary mechanism for improving carrier transport in this photoanode for solar fuels production. The present work establishes the generality of improving photoelectrochemical performance through co-alloying with a transition metal electron donor and a structure-modulating rare earth. Further improvement for all such alloys is obtained by annealing the oxide materials in H_2, ultimately producing photoanodes with above 3 mA cm^{-2} photocurrent density under AM 1.5G illumination, in the top tier of compact $BiVO_4$ films.**

Establishing an efficient photoelectrochemical (PEC) solar fuels technology for renewable energy capture and storage requires several key advancements including the development of an efficient, stable, and inexpensive oxygen evolution reaction (OER) photoanode.[1] Such an advancement would contribute to realizing the solar-driven electrochemical conversion of H_2O and CO_2 into chemical fuels, which offer high energy density and ease of energy storage and distribution. Efforts to improve the promising photoanode material m-$BiVO_4$ (clinobisvanite) by the incorporation of various alloying elements have been attempted with an expansive set of elements and preparation techniques, including combinatorial vapor and liquid phase approaches. The most conclusive result from this work is the increase in electron conductivity from Mo and/or W substitution for V.[2–5] Other strategies for improving m-$BiVO_4$ include nano-structuring, heterojunction formation, hydrogen annealing, and surface coating/passivation,[6–10] and to achieve optimal performance multiple optimization approaches must often be employed in concert.[11] Finding optimal combinations of alloying elements is particularly challenging due to the high dimensionality of the associated composition spaces.[4,5] Our initial combinatorial exploration of co-alloying (adding 2 alloying elements to m-$BiVO_4$) involved synthesis of a library of 948 unique compositions based on addition of various amounts of P, Ca, Mo, Eu, Gd, and W, as well as their pairwise combinations, to m-$BiVO_4$.[12] The primary discovery from the study was that the synergistic co-alloying with Mo and Gd was demonstrated to lower the monoclinic distortion of the m-$BiVO_4$ structure, which improves hole transport. Importantly, this mechanism is a mode of optimization *via* alloy synergy beyond the well-established improvements to electronic conductivity provided by Mo or W.[2,5,13–19] These results motivate the exploration of additional rare earth elements whose impacts on m-$BiVO_4$ structure modulation in conjunction with transition metals have not been previously reported, as well as investigation of whether complementary optimization strategies such as H_2 annealing can further improve PEC performance of m-$BiVO_4$ photoanodes.

To explore these questions, we apply the previously reported methodology[12] for studying combinatorial alloying into monoclinic $BiVO_4$ where 6 different elements are alloyed into each of 3 different Bi:V stoichiometries (Bi-rich, stoichiometric, and V-rich), as are each of the 15 pairwise combinations of the 6 alloying elements. With systematic variation of the alloy and co-alloy loadings, the influence of each alloying element and combination of elements can be assessed, which is best explored with high throughput experimentation given the lack of models for predicting the photoelectrochemical properties of these complex, multi-cation metal oxides.

Our continued exploration of $BiVO_4$-based alloys in the present work included the synthesis and screening of 2 additional libraries, described in detail in the ESI,† that differ in the choice of alloying elements. The composition libraries were deposited by inkjet printing of metal oxide precursors followed by calcination in pure O_2 for 30 minutes at 565 °C, with one of the libraries additionally processed at 280 °C for 10 minutes in 660 torr of 5% H_2/95% Ar. The thickness of a representative sample (given the

[a] *Joint Center for Artificial Photosynthesis, California Institute of Technology, Pasadena CA 91125, USA. E-mail: gregoire@caltech.edu*
[b] *Future Mobility Research Department, Toyota Research Institute of North America, Ann Arbor MI 48105, USA*
[c] *Joint Center for Artificial Photosynthesis, Lawrence Berkeley National Laboratory, Berkeley, CA, 94720, USA*
[d] *Chemical Sciences Division, Lawrence Berkeley National Laboratory, Berkeley, CA 94720, USA*

† Electronic supplementary information (ESI) available: PEC and structural data.

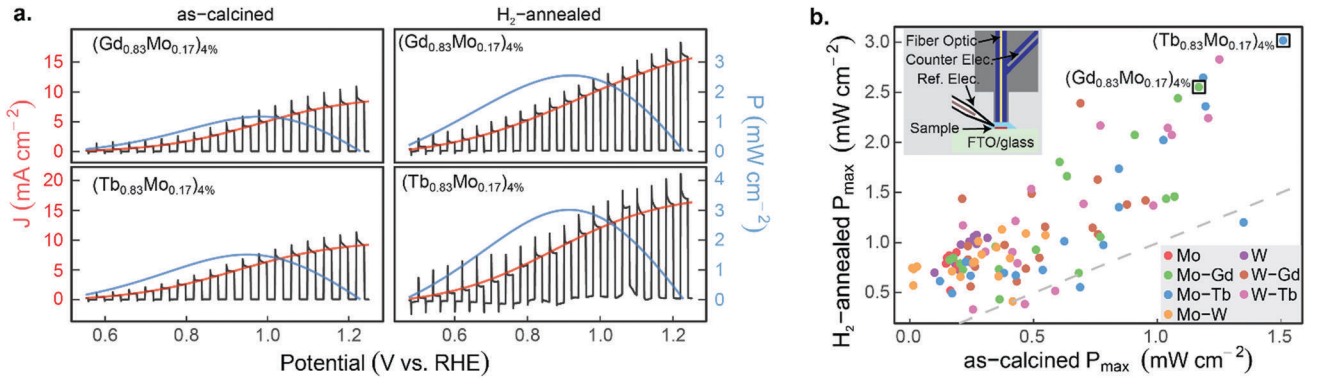

Fig. 1 (a) The raw data (anodic CV sweep with chopped 455 nm illumination, 413 mW cm^{-2}) from 2 representative co-alloy compositions with 4% alloy loading, along with the modeled photocurrent and power densities. (b) The photoelectrochemical power generation of 105 $BiVO_4$ alloy compositions with the noted elements, both without (as-calcined) and with H_2 processing. The gray dashed line corresponds to equal P_{max} values, revealing the universal performance enhancement from hydrogen incorporation. The inset shows a schematic of the PEC cell with 0.581 mm^2 illumination of the ~1 mm^2 samples. The black boxes denote the samples in (a) which were the compositions scaled up.

similar molar loading in each sample) from a duplicate library was about 100 nm by cross sectional SEM (Fig. S2, ESI†).[12] Representative PEC characterization of each sample is illustrated in Fig. 1a where the anodic sweep (20 mV s^{-1}) (see Fig. S3, ESI† for initial cathodic sweeps) of a chopped-illumination cyclic voltammogram (CV) in 0.1 M potassium phosphate aqueous electrolyte (pH 7.2) is modelled to establish the photocurrent density–electrochemical potential (J–E) curve, which provides the OER photoelectrochemical power generation and its maximum value (P_{max}). Given its reliance on photovoltage and photocurrent, this P_{max} value serves as a figure of merit that we aim to improve through optimization of the alloying and thermal processing parameter spaces.

While these experiments provide a wealth of data, we focus here on the most pertinent observations: (i) Mo–Tb and W–Tb co-alloy systems exhibit similar composition–performance relationships as the previously reported Mo–Gd and W–Gd systems and (ii) the H_2 processing results in higher PEC performance over a broad range of alloying compositions, indicating that hydrogen-incorporation provides an improvement mechanism that is complementary to those of the metal alloying elements. The V-rich compositions rarely offer PEC improvement compared to the stoichiometric ($Bi_{0.5}V_{0.5}$) compositions, resulting in our present focus on alloy compositions of the form $Bi_{0.5}V_{0.5}$:$(A_{1-z}Bz)_y$ where y is the total alloy concentration that varies from 0% to 8% and z denotes the relative concentration of the 2 alloying elements in the co-alloy composition spaces (see also Fig. S4, ESI†). As described previously,[12] all compositions are reported by their approximate intended compositions.

Fig. 1a shows the improved PEC performance with H_2 annealing for select Mo–Gd and Mo–Tb samples, for which the P_{max} approximately doubles upon H_2-processing. To characterize the universality of this improvement over different alloying compositions, Fig. 1b compares the P_{max} with and without H_2-processing using 105 compositions from the respective libraries. Photoanode performance greater than approximately 2 mW cm^{-2} is measured from hydrogen annealed Mo–Gd, Mo–Tb, W–Gd, and W–Tb co-alloys. Through photoluminescence[20] and time resolved microwave conductivity[21] measurements, H_2 processing has been shown to passivate native defects, increase n-type doping, and increase carrier lifetime, which is complementary to the metal alloying, in excellent agreement with the observation from Fig. 1b that the H_2 processing improves P_{max} for a broad range of alloy compositions.

The select Mo–Gd and Mo–Tb samples from Fig. 1a are noted in Fig. 1b by black boxes, and to validate the high throughput screening results, each of these compositions were scaled up *via* spin coating of solutions containing the same precursors used in inkjet printing. Following calcination, H_2 processing, and physical characterization (see Fig. S5–S9 and S11, ESI†) a portion of the $Bi_{0.481}V_{0.478}Mo_{0.0068}Gd_{0.034}O_{4+\delta}$ sample was dissolved in 35 vol% HNO_3 for inductively coupled plasma mass spectrometry (ICPMS) composition measurement, yielding the stoichiometry $Bi_{0.471}V_{0.491}Mo_{0.007}Gd_{0.031}$, in good agreement with the intended composition, with the only significant deviation being the slight excess V likely resulting from volatilization of some Bi during annealing.

The scaled-up Mo–Gd composition, both as-calcined and H_2-annealed, was validated and evaluated for operationally stability with a 30 minute chronoamperometry experiment using the same chopped-illumination electrochemistry described above. The results in Fig. S8 (ESI†) show that H_2 annealing produces an initial 3-fold improvement in current density which increases to 3.7-fold over the 30 minute measurement, due to the superior photocurrent stability of the H_2-annealed sample. This experiment demonstrates that the scaled-up compositions perform similarly to the library samples under the high throughput test conditions and that H_2 annealing may improve operational stability.

Spin coated samples were approximately 330 nm thick by cross-sectional SEM (Fig. S5, ESI†), thicker than printed samples. Epoxy-encapsulated electrodes with electrolyte-exposed areas of 0.457 cm^2 (Mo–Gd) and 0.387 cm^2 (Mo–Tb) were used to measure CVs both in the dark and under AM 1.5G illumination (Fig. 2). Given the indication from previous work that these alloying elements effect the bulk carrier transport properties more than the catalytic activity or semiconductor–liquid junction,

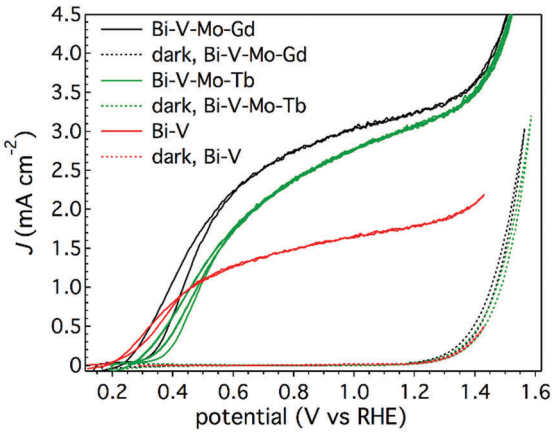

Fig. 2 CVs of scaled up electrodes including the 2 compositions from Fig. 1 and an alloy-free $BiVO_4$ electrode, with 2 cycles both in the dark and under AM 1.5G illumination.

we performed the measurements on scaled-up samples with the addition of 1 M sodium sulfite, which serves as a sacrificial hole acceptor and provides the limiting PEC performance without OER catalysis limitations. The backside illuminated *J–E* curves in Fig. 2 reveal that Mo–Gd and Mo–Tb samples offer substantial improvement compared to non-alloyed, as-calcined $BiVO_4$. The photocurrent densities at 1.23 V *vs.* RHE, which is the most common metric for comparison of $BiVO_4$-based photoanodes, are 3.3, 3.1 and 1.8 mA cm^{-2} for the Mo–Gd, Mo–Tb, and non-alloy sample, respectively. Comparison with previous reports of compact $BiVO_4$ films employing alloying and/or H_2 processing is somewhat challenging given that most optimized electrodes include "catalyst" coatings that have been shown to serve a variety of roles beyond catalysis and are thus not directly comparable to non-coated electrodes measured with a hole scavenger.[22,23] For non-coated films, reported high performance electrodes employ Mo-alloying (1.9 mA cm^{-2}),[24] Mo-alloying with H_2 processing (2.5 mA cm^{-2}),[11] and N_2 processing (3.0 mA cm^{-2}).[25] Upon addition of optimized coatings, the current densities for these electrodes increase to 4.6, 4.9 and 5.0 mA cm^{-2}, respectively, making our 3.3 mA cm^{-2} with Mo–Gd alloying and H_2-processing a top-tier photoanode that may be further improved with an optimized coating. We also measured this Mo–Gd electrode with 2 additional illumination configurations as shown in Fig. S9 (ESI†). Front side illumination provides a similar CV with 3.1 mA cm^{-2} at 1.23 V *vs.* RHE. With the addition of a Ag mirror placed behind the thin film sample in the PEC cell that reflects back transmitted light, the electrode exhibited a substantially higher current of 4.3 mA cm^{-2} at 1.23 V *vs.* RHE. These illumination results indicate that bulk carrier transport does not limit performance, given the co-alloying and H_2 processing-based improvements, but that light harvesting is the performance limiting phenomenon which would need to be addressed *via* thickness optimization and device design.

Given the similar behavior of the Mo–Gd and Mo–Tb samples in both the high throughput and AM 1.5G measurements, we return to evaluation of the conclusion from previous work that the effect of the rare earth is to lower the monoclinic distortion of m-$BiVO_4$ and thereby increase hole transport. Given this understanding of the materials science underpinnings of the PEC enhancement, similar improvements may be found with either Mo or W transition metals (TM) as the electron donor and perhaps any rare earth (RE) as the co-alloying element. Exploration of additional TM–RE combinations was used to test this hypothesis. This exploration proceeded with H_2-processed libraries using Mo–W–Gd–Tb–Dy–Er as the set of 6 alloying elements using the same combinatorial synthesis and screening described above. Additional characterization on these samples (Fig. S10 and S11, ESI†) was also performed to confirm that the H_2 processing does not noticeably alter the optical properties or monoclinic distortion of the co-alloyed samples, as expected from a recent report that H_2 processing has no influence on the Raman signal of m-$BiVO_4$.[21]

Raman analysis of 6 different TM–RE systems with 8% alloy loading are shown in Fig. 3a, with systematic compositional modulation of vibrational modes confirming that the added elements are indeed alloying into m-$BiVO_4$. This relatively high alloy loading was chosen because there is a series of 11 co-alloying

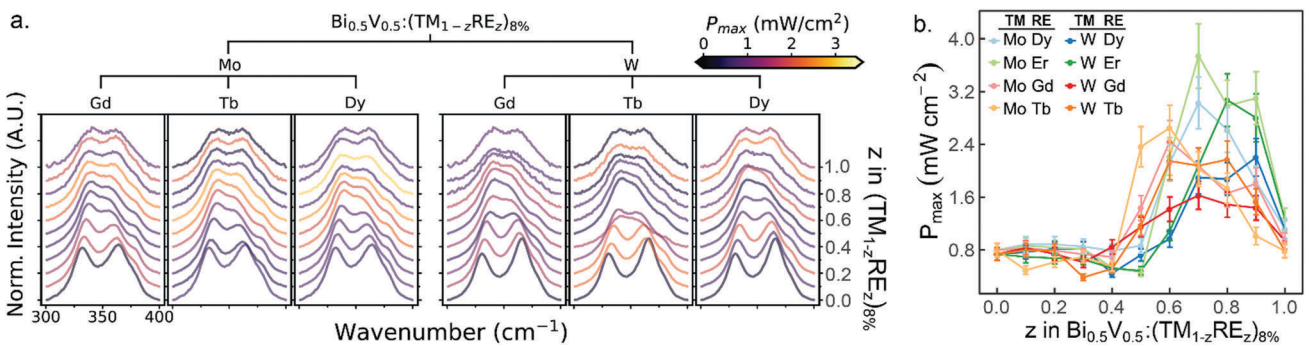

Fig. 3 (a) For each of the 6 co-alloy systems combining a TM and a RE, the Raman signal from VO_4^{3-} bending modes is shown for the series of 11 compositions with end members spanning 8% TM alloying (bottom) to 8% RE alloying (top), revealing that RE alloying leads to merging of the symmetric and antisymmetric modes and that the lowest peaks splitting is observed near 2 : 1 RE : TM. (b) The P_{max} values from H_2 annealed samples measured on duplicate compositions that additionally include Er, revealing that in each co-alloy system select co-alloy compositions outperform the end-member composition that contain a single alloying element. The error bars correspond to 15% relative error that represents variations in synthesis and measurement as quantified from previous analysis of intended duplicate samples.

ratios for each alloy pair. Raman analysis of Er-containing samples is not shown because the Raman signal is obscured by Er fluorescence. As described previously, the monoclinic distortion is best characterized by the difference in wavenumber between the symmetric (s.) and antisymmetric (as.) bending modes of the VO_4^{3-} structural units, which are distinguishable as separate peaks in m-$BiVO_4$ and merge together as the monoclinic distortion is lowered, ultimately becoming degenerate in the higher-symmetry tetragonal structure.[12,26] Fig. 3a shows that very similar trends are observed for each TM–RE co-alloying space, where the pure RE alloys (upper-most spectrum of each panel) have lower monoclinic distortion than the pure TM alloys (lower-most spectrum), and co-alloyed compositions have the lowest monoclinic distortion as indicated by the merging of the double peaks near 350 cm^{-1}. Furthermore, the spectra are colored according to the P_{max} values measured on a duplicate library, revealing that the high-P_{max} samples in each composition space all exhibit low monoclinic distortion. Further analysis of the underlying compositional variation in P_{max} is shown in Fig. 3b for all 8 TM–RE co-alloying spaces. While the RE–TM systems exhibit some quantitative differences, P_{max} variations with RE–TM composition are very similar and identify about 2% TM and 6% RE as the optimal alloying composition, in excellent agreement with the previous result for the 8% alloy loading with as-calcined Mo–Gd samples.[12] The consistency in the optimal TM–RE composition is well explained by the confluence of complementary alloying-based improvements: (i) approximately 2% TM is sufficient to alleviate electronic conductivity as a limiting factor in PEC performance, which is consistent with previous work that includes additional discussion of the defect chemistry and mechanism for this conductivity improvement;[2–5,17] and (ii) the combination of 2% TM and 6% RE minimizes the monoclinic distortion and maximizes hole transport.

These results, which were uniquely enabled by high throughput combinatorial methods, demonstrate a generalized improvement strategy for monoclinic $BiVO_4$ based on synergistic co-alloying of an electron donating TM (W or Mo) in conjunction with a structure modulating RE (Gd, Tb, Er, or Dy). Additionally, H_2 processing was shown to further improve performance, demonstrating that 3 modes of $BiVO_4$ optimization – electronic conductivity *via* TM alloying, hole transport *via* TM + RE alloying, and carrier lifetime *via* H_2 processing – can be simultaneously incorporated. Optimal compositions identified by high throughput experiments were scaled up for AM 1.5 measurements using facile spin coating of an aqueous solution. The $Bi_{0.480}V_{0.480}Mo_{0.007}Gd_{0.034}O_{4+\delta}$ sample provided photocurrent densities at 1.23 V *vs.* RHE of 3.3 mA cm^{-2} with back-side illumination and 4.3 mA cm^{-2} with additional light harvesting, demonstrating the scalable synthesis of high performance photoanodes to advance solar fuels technologies.

This work is performed by the Joint Center for Artificial Photosynthesis, a DOE Energy Innovation Hub, supported through the Office of Science of the U.S. Department of Energy under Award Number DE-SC00049.

Conflicts of interest

There are no conflicts to declare.

References

1 J. Schneider, D. Bahnemann, J. Ye, G. Li Puma and D. D. Dionysiou, *Photocatalysis: Fundamentals and Perspectives*, The Royal Society of Chemistry, 2016, pp. 425–436, DOI: 10.1039/9781782622338.
2 S. P. Berglund, A. J. Rettie, S. Hoang and C. B. Mullins, *Phys. Chem. Chem. Phys.*, 2012, **14**, 7065–7075.
3 R. Gutkowski, C. Khare, F. Conzuelo, Y. U. Kayran, A. Ludwig and W. Schuhmann, *Energy Environ. Sci.*, 2017, **10**, 1213–1221.
4 H. S. Park, K. E. Kweon, H. Ye, E. Paek, G. S. Hwang and A. J. Bard, *J. Phys. Chem. C*, 2011, **115**, 17870–17879.
5 C. Jiang, R. Wang and B. A. Parkinson, *ACS Comb. Sci.*, 2013, **15**, 639–645.
6 Z. F. Huang, L. Pan, J. J. Zou, X. Zhang and L. Wang, *Nanoscale*, 2014, **6**, 14044–14063.
7 H. L. Tan, R. Amal and Y. H. Ng, *J. Mater. Chem. A*, 2017, **5**, 16498–16521.
8 Y. Park, K. J. McDonald and K. S. Choi, *Chem. Soc. Rev.*, 2013, **42**, 2321–2337.
9 B. Lamm, B. J. Trześniewski, H. Döscher, W. A. Smith and M. Stefik, *ACS Energy Lett.*, 2017, **3**, 112–124.
10 K. Tolod, S. Hernández and N. Russo, *Catalysts*, 2017, **7**, 13.
11 J. H. Kim, Y. Jo, J. H. Kim, J. W. Jang, H. J. Kang, Y. H. Lee, D. S. Kim, Y. Jun and J. S. Lee, *ACS Nano*, 2015, **9**, 11820–11829.
12 P. F. Newhouse, D. Guevarra, M. Umehara, S. E. Reyes-Lillo, L. Zhou, D. A. Boyd, S. K. Suram, J. K. Cooper, J. A. Haber, J. B. Neaton and J. M. Gregoire, *Energy Environ. Sci.*, 2018, **11**, 2444–2457.
13 W. Yao, H. Iwai and J. Ye, *Dalton Trans.*, 2008, 1426–1430, DOI: 10.1039/b713338c.
14 J. A. Seabold, K. Zhu and N. R. Neale, *Phys. Chem. Chem. Phys.*, 2014, **16**, 1121–1131.
15 K. P. Parmar, H. J. Kang, A. Bist, P. Dua, J. S. Jang and J. S. Lee, *ChemSusChem*, 2012, **5**, 1926–1934.
16 V. Nair, C. L. Perkins, Q. Lin and M. Law, *Energy Environ. Sci.*, 2016, **9**, 1412–1429.
17 F. F. Abdi, T. J. Savenije, M. M. May, B. Dam and R. van de Krol, *J. Phys. Lett.*, 2013, **4**, 2752–2757.
18 B. Pattengale and J. Huang, *Phys. Chem. Chem. Phys.*, 2016, **18**, 32820–32825.
19 B. Pattengale, J. Ludwig and J. Huang, *J. Phys. Chem. C*, 2016, **120**, 1421–1427.
20 J. K. Cooper, S. B. Scott, Y. Ling, J. Yang, S. Hao, Y. Li, F. M. Toma, M. Stutzmann, K. V. Lakshmi and I. D. Sharp, *Chem. Mater.*, 2016, **28**, 5761–5771.
21 J.-W. Jang, D. Friedrich, S. Müller, M. Lamers, H. Hempel, S. Lardhi, Z. Cao, M. Harb, L. Cavallo, R. Heller, R. Eichberger, R. van de Krol and F. F. Abdi, *Adv. Energy Mater.*, 2017, **7**, 1701536.
22 D. Guevarra, A. Shinde, S. K. Suram, I. D. Sharp, F. M. Toma, J. A. Haber and J. M. Gregoire, *Energy Environ. Sci.*, 2016, **9**, 565–580.
23 C. Zachäus, F. F. Abdi, L. M. Peter and R. van de Krol, *Chem. Sci.*, 2017, **8**, 3712–3719.
24 M. Rohloff, B. Anke, S. Zhang, U. Gernert, C. Scheu, M. Lerch and A. Fischer, *Sustainable Energy Fuels*, 2017, **1**, 1830–1846.
25 T. W. Kim, Y. Ping, G. A. Galli and K.-S. Choi, *Nat. Commun.*, 2015, **6**, 8769.
26 D. Zhou, L.-X. Pang, H. Wang, J. Guo, X. Yao and C. A. Randall, *J. Mater. Chem.*, 2011, **21**, 18412.